

Research Article

Estimation of Grain Orientation in an Anisotropic Weld by Using a Model of Ultrasonic Propagation in an Inverse Scheme

Qingwei Liu¹ and Håkan Wirdelius²

¹ Aker Solutions, P.O. Box 73, 3401 Lier, Norway

² SCeNDT, Department of Materials and Manufacturing Technology, Chalmers University of Technology, 412 96 Gothenburg, Sweden

Correspondence should be addressed to Håkan Wirdelius; hakan.wirdelius@chalmers.se

Received 25 February 2014; Revised 11 June 2014; Accepted 12 June 2014; Published 1 July 2014

Academic Editor: Mohamed B. Trabia

Copyright © 2014 Q. Liu and H. Wirdelius. This is an open access article distributed under the Creative Commons Attribution License, which permits unrestricted use, distribution, and reproduction in any medium, provided the original work is properly cited.

The initial step towards a nondestructive technique that estimates grain orientation in an anisotropic weld is presented in this paper. The purpose is to aid future forward simulations of ultrasonic NDT of this kind of weld to achieve a better result. A forward model that consists of a weld model, a transmitter model, a receiver model, and a 2D ray tracing algorithm is introduced. An inversion based on a multiobjective genetic algorithm is also presented. Experiments are conducted for both P and SV waves in order to collect enough data used in the inversion. Calculation is conducted to fulfill the estimation with both the synthetic data and the experimental data. Concluding remarks are presented at the end of the paper.

1. Introduction

Ultrasonic nondestructive testing (NDT) is widely applied in industry. This attributes to the fact that ultrasound can detect, characterize, and size defects, in a component, while the propagation of ultrasound through the tested part does not affect the workpiece's future functionality.

On the path of ultrasound propagation, if there is a discontinuity in the medium's elastic properties, the amplitude, phase, and the direction of the ultrasound are affected. When the ultrasound is detected by the receiver, the change of the medium's property is reflected by the receiver's output. In this sense, ultrasound is an agent that can convey information on the path from a transmitter to a receiver. The characteristic of being an information carrier also makes ultrasound suitable in the application of a medium's property measurement, for example, in the determination of elastic constants in materials.

In the area of material science, the determination of elastic properties for a specific composite material is essential. In many cases, an ultrasonic NDT technique is applied and a direct measurement of ultrasound velocity is performed. Wang [1] presented a method to recover elastic constants

from group velocity measurements in two dimensions, with an intention to make the method applicable even to the three-dimensional case. In contrast to Wang [1], Aristégui and Baste [2] presented a method that makes use of phase velocity measurement for optimal identification of material symmetry and independent elastic constants in a homogeneous anisotropic solid. Degtyar and Rokhlin [3] introduced an inversion procedure based on a nonlinear least-squares method to determine elastic constants from group or phase velocity data in orthotropic and transversely isotropic materials.

Correspondingly, in the area of conventional ultrasonic NDT, the elastic properties of the addressed component are also key factors. This is due to the fact that the medium's elastic properties will influence its sound propagation properties and therefore influence both theoretical simulation and practical testing. In many applications within the nuclear power industry, defects in components or in the region of austenitic welds are assessed by using ultrasonic NDT. Since these welds tend to exhibit strong anisotropy, problems with the interpretation of received signal have been reported. When applying ultrasonic NDT to test their integrity, the propagation of ultrasound is significantly different from that

in an isotropic medium. It is indicated by the fact that wave velocities become directionally dependent; group and phase velocities are no longer necessarily parallel or equal in magnitude [4].

Therefore, research on the propagation of ultrasound through an anisotropic weld has attracted many researchers' attention [4–9]. The assumption of the weld being two-dimensional and transversely isotropic is often used [10, 11] and has recently also been experimentally validated [12]. In a more recent work [13] a phased array pitch-catch system is modelled by sequential point sources. Even though ray tracing and discretization resemble this work the inversion scheme is based on huge amount of data as time traces using Monte Carlo simulations. In most simulation cases, a simple weld model is created by studying the macrograph of an austenitic weld. Different algorithms are then utilized to simulate the propagation of ultrasound through weld models. Among the studies, there exists a different method, not using a macrograph, to establish a weld model used in simulations. Apfel et al. [14] and Gueudre et al. [15] have created models by considering the welding process. In their models, the grain's orientation at different positions is decided by several parameters such as the chamfer geometry, the number of passes, and the diameter of electrodes. After that, an ultrasonic wave propagation code in finite element method is applied to deduce the propagation of ultrasound. It is worth mentioning that an inverse calculation is taken into consideration in their study. By comparing the modeling results with the experimental ones, modeling parameters can be optimized by an iterative loop. Consequently, better grain orientations are achieved.

In this paper, a similar effort is made with the purpose of estimating the grain orientation in an anisotropic austenitic weld. In the study, the weld is divided into around eighty subregions. Each subregion is supposed to be homogeneous and transversely isotropic with its own crystal orientation θ_i . Combined with a ray tracing algorithm and experimental data, optimization calculations are utilized to further estimate these orientations (see Figure 1) rather than the model parameters used by Apfel et al. [14] or Gueudre et al. [15].

Obviously, such an effort is composed of a forward model and an inverse calculation. The forward model realizes a theoretical simulation, which determines paths of ultrasonic energy through a weld model, as well as the detection of the maximum output at the receiver. The inverse calculation is fulfilled by an optimization algorithm, which presents the optimal estimation of the crystal orientations by minimizing the difference between the simulation data and the experimental results. In this paper, the forward model is introduced in Section 2. It consists of a weld model, a transmitter model, a receiver model, and a 2D ray tracing model. In Section 3, the inverse problem is briefly reviewed and a multiobjective genetic algorithm is employed to conduct the inversion. Inversion with synthetic data is performed in Section 4. Experiment on a specific weld is introduced in Section 5, which is followed by the inversion calculation with different combination of experimental data. Concluding remarks and discussions are presented in the last section.

2. Forward Model

To establish a forward model, each element of the system is abstracted to a mathematical description. Then the output of the whole system is obtained on condition that a proper input is supplied to the model. Obviously, simulation results depend heavily on the accuracy of the model, as well as how closely the model approaches reality. In this paper, the forward model is implemented by a 2D ray tracing algorithm running on a weld model. The forward model then consists of a model of the weld, a model of the transmitter, a model of the receiver, and a ray tracing model. The piecewise two-dimensionality is assessed by the ultrasonic procedure that specifies the measurement in a line-scan perpendicular to the weld.

The weld model is created by analyzing the macrograph of a specific austenitic weld, which is shown in Figure 2. The determination of the subregions and the crystal orientations is described in a previous paper [16]. The weld model created is shown in Figure 3 and it consists of the base materials and eighty smaller weld subregions.

As to the weld specimen used in this paper, the base materials are stainless steel X10CrNiNb189 (AISI 347), while the welding material is stainless steel X1CrNi19-9 (AISI 308L). In the modeling, the base material is supposed to be isotropic with Lamé constants $\lambda_L = 109$ GPa and $\mu_L = 79$ GPa. The density is $\rho = 8.02 \times 10^3$ kg/m³. In the welded area, each subregion is assumed homogeneous and transversely isotropic and has its own unique crystal orientation. For the elastic constants utilized in the simulation, the elements of the stiffness matrix are $c_{11} = 249$ GPa, $c_{12} = 112$ GPa, $c_{13} = 145$ GPa, $c_{33} = 216$ GPa, and $c_{44} = 129$ GPa. The density is assumed to be $\rho = 8.30 \times 10^3$ kg/m³ [17]. As observed from Figures 2 and 3, the dimension of the weld model is slightly modified from its prototype with a purpose of simplifying the forward simulation. The dimension of the weld model used in this paper is based on previous report [17] which includes the chosen discretization of the weld, that is, maximum number of subregions or dendrite formations in these four welds. The lengths are based on one of these with the upper width as 18 mm, the lower width as 13 mm, and the height as 22 mm.

The transmitter model is realized from a truncated traction distribution over a half-space. First, a plane wave is supposed to propagate at a certain direction in the half-space. Then the corresponding traction distribution at the top of the half-space is determined. In the frequency domain, the traction distribution is further truncated to the size of the probe. Then the truncated traction distribution is considered to be generated by a transmitter. Both P and SV wave fields can be calculated with this transmitter model. Previous simulations prove that, in the far field, the wave generated by this transmitter model can be taken as a plane wave locally.

In the process of simulation, a transmitter-receiver form of pitch-catch is supposed. A receiver model is then implemented using Auld's electromechanical reciprocity principle [18]. In simulating the receiver, two different states of the system are considered. State 1 is the testing state. Here, the transmitter is at the working position; the weld and the lower backwall act as a scatterer. In state 2, the transmitter is put

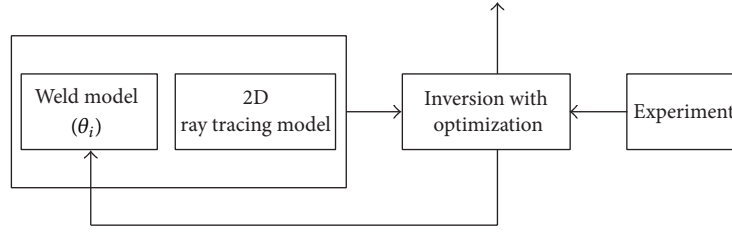


FIGURE 1: Block diagram of the idea.

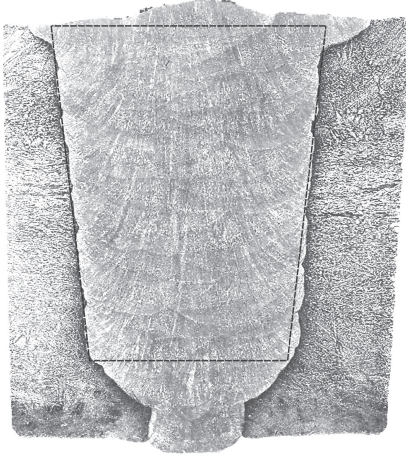


FIGURE 2: The macrograph of weld B27.

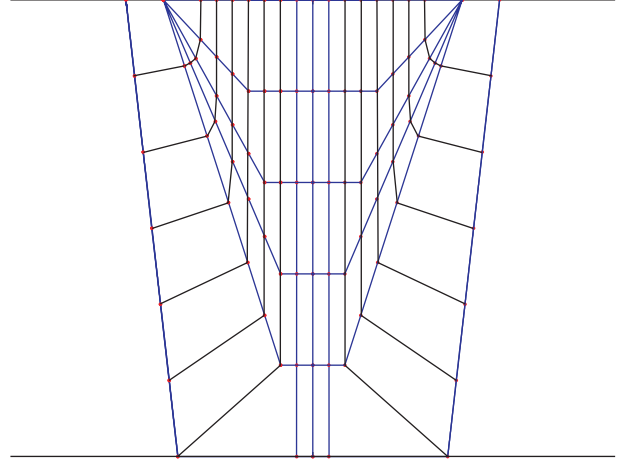


FIGURE 3: The weld model created.

at the receiver's position as in state 1. Moreover, the scatterer is absent in this state; that is, the ultrasound is transmitted into a homogeneous half-space with the material parameters of the base material. The change in the electrical transmission coefficient is calculated by

$$\delta\Pi = \frac{i\omega}{4P} \int_{\Gamma} (\mathbf{u}_2 \cdot \mathbf{t}_1 - \mathbf{u}_1 \cdot \mathbf{t}_2) d\Gamma. \quad (1)$$

In this expression, ω is the angular frequency and P is the probe electrical power. \mathbf{u}_i ($i = 1, 2$) is the displacement vector for state 1 or 2. \mathbf{t}_i ($i = 1, 2$) is the traction vector corresponding to state 1 or 2, respectively. Γ is the boundaries enclosing the scatterer.

To establish the 2D ray tracing model, the algorithm used in, for example, RAYTRAIM [4, 19] is chosen. A similar 2D ray tracing model was recently validated by using EFIT calculations [20] with very good agreement. In simulating the propagation of ultrasound through the weld model, the ultrasonic beam is approximated for high frequencies as a ray. The direction of the ultrasonic energy is continuously followed. Transmission and reflection are considered on the fusion lines between the base material and the weld, as well as on the boundaries between the subregions in the weld. In the simulation, no mode conversion between the P wave and the SV wave is considered. This can be experimentally assessed by gating out the received information in thoroughly chosen time window. As a consequence, only the wave with the same mode is traced from the transmitter to the receiver.

A model that prescribes the signal response based on the propagation of ultrasound from a transmitter, through a weld, and then to a receiver is constructed. The forward simulation results can then be utilized in an inversion calculation to optimize the crystal orientations in a weld.

3. The Inverse Algorithm

An inversion is usually applied to determine quantities that are difficult or impossible to measure directly from attainable parameters. Strictly speaking, ultrasonic NDT itself is a process of inversion because the integrity of a workpiece or the existence of a flaw can only be evaluated from the ultrasound output. Undoubtedly, this inversion task needs a proper technique and qualified experience. The inversion performed in this paper is a process of parameter identification. It is aimed at estimating the grains' crystal orientations in an austenitic weld using both theoretical simulations and groups of experimental data.

Here, an optimization algorithm is applied to perform the inversion. The objective of the optimization is to minimize the difference between the simulation results and the experimental data. In a previous paper [21], the applicability of two different optimization methods, which are a local optimization method and a global optimization method, has been discussed. For the weld model used in this paper, the presentation of all necessary constraints demanded by an inversion with local optimization is difficult; therefore

a global optimization method based on the genetic algorithm becomes the choice. When considering various objectives simultaneously, a multiobjective genetic algorithm [22] is adopted, which can be described by

$$\text{Minimize } \mathbf{f} = [f_1, f_2, \dots, f_n]^T. \quad (2)$$

Here, f_i ($i = 1, 2, \dots, n$) are different objectives in a set \mathbf{f} . The objectives in this paper are the position difference of the maximum signal, between the detected and the simulated results. This is

$$f_i = |y_{\max}^{\text{sim}} - y_{\max}^{\text{exp}}|. \quad (3)$$

In this expression, y is the position of maximum signal. Superscripts *sim* and *exp* indicate that the quantity corresponds to the simulation or experimental result. The concept of Pareto optimality is applied to define the optima. This is an optimization method making compromises between different objectives and finally presenting many alternatives that can compete with each other. This kind of optima coincides with the property of multisolution in a nonlinear inversion.

In this paper, the inversion is not performed on every subregion's crystal orientation. This means that the subregions with a grain orientation of 90° to the positive direction of the x_1 axis will not be estimated by the inversion because these subregions are located in the middle of the weld specimen and their grain orientations are believed to be close to reality. As a consequence, there are 34 variables needed to be determined. If the assumed symmetry of the subregions in the weld model is considered, the number of variables to be determined will further decrease to 17.

This is illustrated in Figure 4. As observed from the figure, the subregions without a label number are believed to have a crystal orientation of 90° . In those subregions with a label 1–17, a crystal orientation of θ_i ($i = 1, 2, \dots, 17$) is to be determined by the inversion. The orientations of the rest of the subregions θ_i ($i = 18, 19, \dots, 34$) are determined by symmetry,

$$\theta_j = 180^\circ - \theta_{(j-17)} \quad (j = 18, 19, \dots, 34). \quad (4)$$

In Table 1, the allowed intervals ($\delta = 10^\circ$) of these 17 variables in the simulations are presented. Their modeled nominal values that are calculated from a previous model in [12] are also provided in the table.

4. Inversion with Synthetic Data

Before proceeding to the experiment and the inversion with true data, synthetic data are generated to test the whole system. Only data from the P wave probes are created by the forward model. Both 45° and 60° measurement systems are simulated. The data created are shown in Table 2.

Totally there are 34 pairs of data, 19 pairs from the 45° system and 15 pairs from the 60° system. In each pair, the position of the transmitter that is denoted by x is given as an input parameter to the forward simulation. Then the position

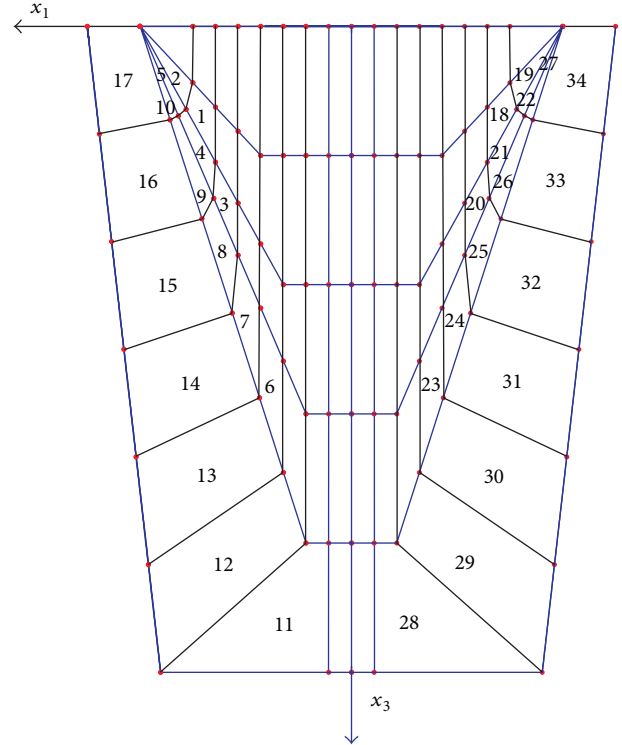


FIGURE 4: Subregions having a grain orientation to be determined in the inversion.

of the receiver at the maximum signal that is indicated by y is calculated by the program. Both x and y are measured from the central line of the weld. A sketch in Figure 5 clarifies the parameters in the measurement system.

It is noticed from the table that y values are all integers. This is caused by the simulation algorithm used in the receiver model. There, the receiver is modeled to move in an interval of 1 mm. In addition, the synthetic data are free from noise. The purpose is to check if the inversion can find the right solution with these clean data. If it cannot locate the right solution within reasonable steps, this will demonstrate the difficulty of the nonlinear inversion.

In Figure 6, a picture of the weld model covered by the rays of these synthetic data is displayed. It is observed that some subregions and their symmetric subregions are not covered by any rays, for example, numbers 1, 2, 5, and 10. This will make the inversion results of these subregions meaningless.

The inversion is realized by a multiobjective genetic algorithm—NSGA-II [23]. The algorithm initially creates a parent generation randomly with a population of N individuals. Each individual is assigned a rank corresponding to its nondomination level. The selection, crossover, and mutation operators are performed to create a child population. The combination of the parent and the child population is sorted again according to the nondomination principle. The preceding N individuals are chosen to carry out selection, crossover, and mutation to create a new child population. Further, the whole procedure is repeated until the algorithm is finished.

TABLE 1: Nominal values of the 17 variables and their allowed intervals ($\delta = 10^\circ$) ($^\circ$).

	θ_1	θ_2	θ_3	θ_4	θ_5	θ_6	θ_7	θ_8	θ_9
Nominal	85.29	75.75	88.87	77.46	40.08	89.60	87.14	77.18	50.70
Max	90.00	80.00	93.00	82.00	45.00	94.00	92.00	82.00	55.00
Min	80.00	70.00	83.00	72.00	35.00	84.00	82.00	72.00	45.00
	θ_{10}	θ_{11}	θ_{12}	θ_{13}	θ_{14}	θ_{15}	θ_{16}	θ_{17}	
Nominal	26.28	60.61	38.24	30.32	22.37	16.51	12.85	6.47	
Max	31.00	65.00	43.00	35.00	27.00	21.00	18.00	11.00	
Min	21.00	55.00	33.00	25.00	17.00	11.00	8.00	1.00	

TABLE 2: Synthetic data generated by the forward simulation (mm).

		45°									
x	12.0	13.0	14.0	15.0	16.0	17.0	18.0	19.0	20.0	21.0	
y	33.0	18.0	25.0	24.0	25.0	21.0	17.0	33.0	26.0	24.0	
		45°									
x	22.0	23.0	24.0	25.0	26.0	27.0	28.0	29.0	30.0		
y	22.0	22.0	18.0	21.0	21.0	22.0	20.0	17.0	15.0		
		60°									
x	12.0	16.0	18.0	22.0	24.0	26.0	30.0	31.0	32.0	34.0	
y	54.0	57.0	55.0	56.0	54.0	50.0	52.0	51.0	50.0	28.0	
		60°									
x	36.0	38.0	40.0	42.0	44.0						
y	30.0	30.0	29.0	28.0	17.0						

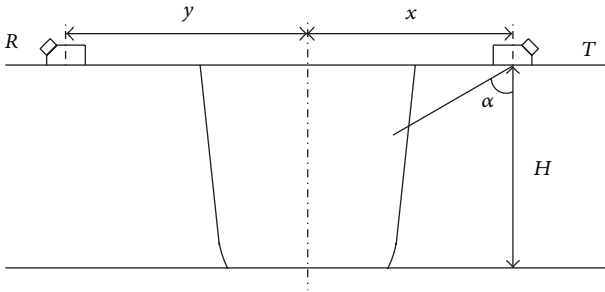


FIGURE 5: Parameters in the measurement system.

The inversion with synthetic data runs 60 generations, each with an individual number of $N = 80$. Strictly speaking, the result of the inversion does not give very satisfactory results. Many solutions can compete with each other on satisfying the objectives and it is hard to point out which is the single best result. This is believed to coincide with the property of multisolution in a nonlinear inversion. Considering the 80 individuals in the last generation, three better candidates can be located. They are shown in Table 3. The corresponding averaged residue sums ($(1/n) \sum_{i=1}^n f_i$) of the objectives are 2.35 mm, 2.38 mm, and 3.00 mm, respectively. Here, $n = 34$. It is reasonable to think that a larger generation number may possibly present better results. But since the synthetic data without noise are used, it should be enough to characterize the difficulty of the problem with a smaller

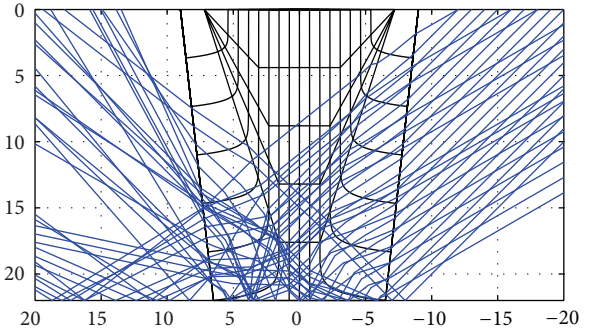


FIGURE 6: The weld model is covered by rays of synthetic data.

number. As shown in the table, the biggest dispersion of each variable among the three individuals appears on θ_4 with a value of 7.6° . The others are within 6° . To a large extent, these results may be acceptable though there is no individual presenting results that are exactly the same as the nominal values in Table 1.

In order to investigate the influence of allowed intervals of the variables to the dispersion, the same simulation is repeated, but with a wider allowed interval on each variable. The intervals are broadened on both the max and the min sides with 5° ($\delta = 20^\circ$ totally). One exception is θ_{17} that changes from 1.00° to 16.00° instead. Table 4 lists the enlarged interval of each variable.

TABLE 3: Three groups of better result in the last generation when using synthetic data (variables varied within $\delta = 10^\circ$) ($^\circ$).

	θ_1	θ_2	θ_3	θ_4	θ_5	θ_6	θ_7	θ_8	θ_9
Individual 1	85.73	79.44	92.27	77.51	43.91	89.88	86.32	81.54	49.14
Individual 2	88.87	78.31	92.48	80.51	42.70	88.79	91.23	79.23	48.46
Individual 3	89.70	70.78	92.88	72.91	38.15	89.59	89.49	76.71	52.44
	θ_{10}	θ_{11}	θ_{12}	θ_{13}	θ_{14}	θ_{15}	θ_{16}	θ_{17}	
Individual 1	27.93	60.64	37.27	31.93	20.71	19.35	15.52	7.70	
Individual 2	27.04	62.63	37.00	27.99	19.64	20.69	10.00	2.45	
Individual 3	22.82	64.94	36.99	29.61	19.60	20.60	11.79	2.50	

TABLE 4: Enlarged allowed intervals of the 17 variables ($^\circ$).

	θ_1	θ_2	θ_3	θ_4	θ_5	θ_6	θ_7	θ_8	θ_9
Max	95.00	85.00	98.00	87.00	60.00	99.00	97.00	87.00	60.00
Min	75.00	65.00	78.00	67.00	30.00	79.00	77.00	67.00	40.00
	θ_{10}	θ_{11}	θ_{12}	θ_{13}	θ_{14}	θ_{15}	θ_{16}	θ_{17}	
Max	36.00	70.00	48.00	40.00	32.00	26.00	23.00	16.00	
Min	16.00	50.00	28.00	20.00	12.00	6.00	3.00	1.00	

The first three groups of better result are presented in Table 5. The corresponding averaged residue sum is 1.94 mm, 2.47 mm, and 2.56 mm, respectively. Though the first individual has a smaller averaged residue sum than the other individuals or the individuals in Table 3, it is far from the nominal value in Table 1. The largest difference occurs at θ_{11} with 8.88° . The second largest occurs at θ_3 with a value of 7.29° . Other variables having a difference around 6.00° are θ_4 , θ_7 , θ_{15} , and θ_{17} . Comparing the three individuals in Table 5, it is hard to find an area that a variable can best locate in. The largest dispersion happens on θ_3 with a value of 12.71° , followed by θ_{11} with 12.22° and θ_7 with 11.54° .

It is indicated that the extension of the varying limitations of each variable will present other candidates satisfying the objectives equally well in a larger area. It means that in this nonlinear problem, there are possibly many solutions being able to solve the problem.

In Table 6, the dispersions of each variable obtained from the cases of $\delta = 10^\circ$ and $\delta = 20^\circ$ are compared. The dispersion is calculated with $(\theta_i^{\max} - \theta_i^{\min})$ among the individuals in each case. If θ_1 , θ_2 , θ_5 , and θ_{10} are not considered, it is observed that, with a larger allowed interval, the variables achieved generally have a larger dispersion also. Moreover, this change of the dispersion is fairly obvious. Exceptions occur on variables θ_4 , θ_8 , θ_{12} , θ_{13} , and θ_{17} , while, the dispersion of most of these exceptional variables does not change markedly. This phenomenon indicates that if the analysis of the weld's macrograph is reliable, the allowed interval of each variable in the inversion could be limited within a smaller region. As a result, the inversion will finally present solutions around the nominal values in the weld model.

5. Experiments

The experiments are conducted at the Swedish Qualification Center (SQC). A weld specimen B27 is supplied and prepared by SQC. One side of the weld specimen is machined from its

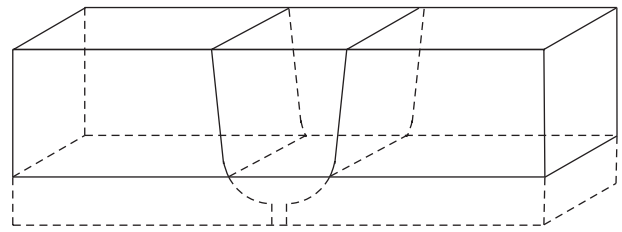


FIGURE 7: The process of preparing the weld specimen for the experiment.

bottom to make it coincide with the weld model shown in Figure 3 which is indicated in Figure 7.

Except for the weld specimen, the whole experimental system is mainly composed of five parts (see Figure 8), which are the ultrasound probes, a set of instruments, a suite of software for both data acquisition and evaluation, manipulator, and motor control. Panametric V-series probes are employed in the experiments, which have crystal size of 13 mm in diameter. The working frequency is 2.25 MHz. Wedges for 45° and 60° P and SV probes are used. The measurement system Tomo SV RD Tech is utilized. Data acquisition is implemented by the software of RD Tech 1.3B3, while evaluation is fulfilled by the software of Zetec Ultra Vision 1.0R5. Manipulator and motor control are realized by AWS-6, Force Technology, and Phoenix PC-Link MCPA2-2, respectively.

As shown in the picture of the measurement system, a pitch-catch testing style of the transmitter-receiver is employed. During one run of the experiment, the transmitter is kept at a fixed distance from the central line of the specimen. The receiver scans in a line that is perpendicular to the weld. This is repeated for a length of 25 mm along the weld with an increment of 5 mm. A C-scan of the weld specimen is then completed. After this run, the whole system is reset to

TABLE 5: Three groups of better result in the last generation when using synthetic data (variables varied within $\delta = 20^\circ$) ($^\circ$).

	θ_1	θ_2	θ_3	θ_4	θ_5	θ_6	θ_7	θ_8	θ_9
Individual 1	87.29	82.03	96.16	71.21	33.96	89.38	81.14	80.50	50.25
Individual 2	90.16	67.46	97.83	71.20	47.69	90.40	92.68	82.49	57.18
Individual 3	87.30	81.07	85.12	77.37	45.11	89.06	82.60	78.07	47.21
	θ_{10}	θ_{11}	θ_{12}	θ_{13}	θ_{14}	θ_{15}	θ_{16}	θ_{17}	
Individual 1	32.83	51.73	38.00	35.96	23.41	22.53	12.20	12.61	
Individual 2	35.40	63.94	37.72	35.08	25.82	20.27	13.75	11.76	
Individual 3	33.39	51.72	38.00	33.73	22.56	22.53	5.72	13.90	

TABLE 6: Comparison of the dispersion of each variable obtained in those two cases $\delta = 10^\circ$ and $\delta = 20^\circ$, synthetic P wave data, ($^\circ$).

	θ_1	θ_2	θ_3	θ_4	θ_5	θ_6	θ_7	θ_8	θ_9
$\Delta\theta_i$ ($\delta = 10^\circ$)	3.97	8.66	0.61	7.60	5.76	1.09	4.91	4.83	3.98
$\Delta\theta_i$ ($\delta = 20^\circ$)	2.87	14.57	12.71	6.17	13.73	1.34	11.54	4.42	9.97
	θ_{10}	θ_{11}	θ_{12}	θ_{13}	θ_{14}	θ_{15}	θ_{16}	θ_{17}	
$\Delta\theta_i$ ($\delta = 10^\circ$)	5.11	4.30	0.28	3.94	1.11	1.34	5.52	5.25	
$\Delta\theta_i$ ($\delta = 20^\circ$)	2.57	12.22	0.28	2.23	3.26	2.26	8.03	2.14	

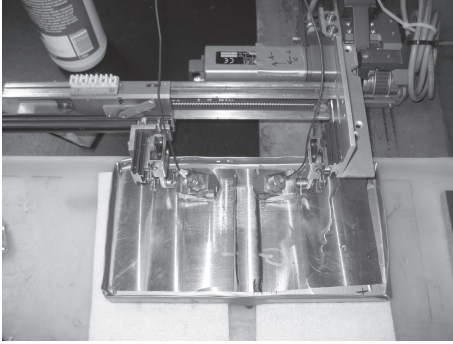


FIGURE 8: Photo of the specimen, scanning probes, and manipulator unit used in the experimental system. Experimental setup.

its original condition and the transmitter is moved to a new position; then the same scan process is repeated. When all the parallel scans are finished, the data processing software presents A-, B-, C-, and D-scan displays.

Both the P wave and the SV wave probes are applied in the experiments, both 45° and 60° for each probe. Totally 31 groups of experiments are obtained, the parameters of which are shown in Tables 7 and 8. The meaning of x and y in the tables is shown in Figure 5.

Some special phenomena that happened in the experiments are worth being mentioned here. First, when determining the peak position in an A-scan, it is hard to locate one precise point because the A-scans display a rather flat curve on their tops. Second, when acquiring data from different sections of a C-scan, usually different peak positions are obtained. Take the transmitter position of 20 mm in the

experiment using the 60° P wave probe as an example; there is a difference of 1.2 mm in read-outs on two different sections. Third, in some cases, two peak positions are displayed even in the scan of one section. For example, when doing experiment with the 45° SV wave probe, two peak positions at 50.5 mm and 55 mm are observed corresponding to the transmitter position of 22 mm. In the experiments for the 60° SV wave probe, the difference between two peak positions can be as large as 20 mm. This may be explained by mode conversions happening during ultrasound propagating through the anisotropic weld. Fourth, it is observed, for example in Table 7, that the peak position does not move monotonously along with the change of the transmitter's position. Jumps between data can also be noticed. This well explains the complexity of ultrasonic NDT experiments. Moreover, it implies the nonlinear property when modeling ultrasound propagating through an anisotropic weld. The typical estimation method used in evaluating ultrasonic measurement on an isotropic medium is not feasible here. As shown in Figure 5, if the medium beneath the probes is isotropic, the distance between the transmitter and the receiver can be estimated by $x + y = 2H \tan \alpha$. In the case of anisotropic media lying under the probes, this expression generally is not valid.

Comparing the simulation data listed in Table 2 and the experimental results in Table 7, it is seen that large discrepancies occur at most of the points. It is noticed that except for the cases of $x = 20.0$ mm, 22.0 mm, and 24.0 mm (45° probe), disparity exists between the simulated and the experimental data. One may take this difference as the objective function in the inversion, but large disparity may also be caused by the imperfection of the forward simulation, as well as possible erroneous experimental data.

TABLE 7: Experimental data of P probe, 2.25 MHz, (mm).

		45°								
x	20.0	22.0	24.0	26.0	28.0	30.0	32.0*			
y	24.0	21.0	21.0	10.0	9.5	8.5	8.5			
		60°								
x	16.0	18.0	20.0	22.0	24.0	26.0	28.0	30.0	32.0	34.0
y	36.9	26.2	26.6	27.5	27.0	26.0	21.0	21.5	20.5	20.5

*Data in bold are used in inversions with P wave only but not in the inversion with a combination of both P and SV waves.

TABLE 8: Experimental data of SV probe, 2.25 MHz, (mm).

		45°							
x	12.0	14.0	16.0	18.0	20.0	22.0	24.0	26.0	
y	35.5	35.0	34.5	33.0	33.5	33.0	31.0	20.5	
		60°							
x	20.0	22.0	25.0	27.0	29.0	30.0			
y	36.0	38.5	41.0	25.0	23.5	22.5			

TABLE 9: Four groups of better result in the last generation, inversion with the P wave experimental data (variables varied within $\delta = 10^\circ$) ($^\circ$).

	θ_1	θ_2	θ_3	θ_4	θ_5	θ_6	θ_7	θ_8	θ_9
Individual 1	85.18	79.64	92.27	78.68	36.08	93.67	91.84	73.83	45.10
Individual 2	85.11	79.78	88.74	76.84	36.63	93.66	91.84	73.87	51.76
Individual 3	85.11	79.54	88.74	76.84	36.63	93.66	91.84	73.87	51.76
Individual 4	85.19	79.69	90.14	78.69	37.34	92.54	91.44	72.88	51.32
	θ_{10}	θ_{11}	θ_{12}	θ_{13}	θ_{14}	θ_{15}	θ_{16}	θ_{17}	
Individual 1	26.21	59.00	39.24	27.53	21.93	19.34	9.65	10.78	
Individual 2	26.07	59.16	33.21	34.25	22.28	16.94	13.06	10.74	
Individual 3	26.07	59.16	33.21	34.25	22.28	16.94	13.06	10.74	
Individual 4	28.34	55.44	33.06	34.25	25.74	15.40	14.62	10.49	

6. Inversions

Two inversions are performed in this section, which use different combinations of experimental data. In the inversion with only P wave results, 80 generations of calculation are performed. In each generation, 80 individuals are generated. In the inversion with both P and SV wave data, the same numbers of generations and individuals are employed. Though these two numbers of generations and individuals can be raised to even larger amount, for example, several hundreds, the time for the inversion calculation will increase accordingly.

6.1. Inversion with P Wave Only. Only the P wave experimental data, which are listed in Table 7, are utilized in the inversion calculation. Thus, there are 17 variables and 17 pairs of experimental data. Correspondingly, there are 17 objectives in the multiobjective optimization.

First, an allowed interval of $\delta = 10^\circ$ is adopted in the inversion. The detailed limitation of each variable is shown in Table 1. It is found that the inversion calculation fails to provide a satisfactory result. If considering similarly the individuals in the last generation, four groups of variables

with a better averaged residue sum are listed in Table 9. The reason for providing four groups of data here is that two of the individuals are almost identical. One more group of data is more convincing. The corresponding values of averaged residue sum are 8.35 mm, 8.76 mm, 8.76 mm, and 8.94 mm.

As observed from the averaged residue sum of the objectives, the result is not satisfactory because the averaged residue sum is as large as almost 9 mm. This may be attributed to the fact that the amount of data is not sufficient. Only 17 pairs of P wave data are utilized. More data may present better results. In addition, SV wave data have not been employed in the inversion. Since the SV wave is more seriously affected by the anisotropy in a weld than the P wave, the inclusion of SV wave data may perhaps give a better result. In addition, the similarity between individuals 2 and 3, which is caused by the truncation of data in display, should not indicate that this is the best solution. The reason is that it is possible that θ_2 is not covered by any ray, which is shown in Figure 6. Hence the tiny difference between these two individuals in θ_2 could be considered as one individual.

Similarly, the calculation is also performed for the case that the allowed interval of each variable is enlarged 5° on both sides of the maximum and the minimum. Consequently,

TABLE 10: Three groups of better result in the last generation, inversion with the P wave experimental data (variables varied within $\delta = 20^\circ$), ($^\circ$).

	θ_1	θ_2	θ_3	θ_4	θ_5	θ_6	θ_7	θ_8	θ_9
Individual 1	77.28	68.60	92.38	71.12	37.33	87.29	92.01	72.77	52.17
Individual 2	75.94	67.92	94.95	73.48	45.46	98.87	92.20	71.82	44.97
Individual 3	76.01	79.91	85.74	70.34	45.59	96.77	93.64	71.83	40.18
	θ_{10}	θ_{11}	θ_{12}	θ_{13}	θ_{14}	θ_{15}	θ_{16}	θ_{17}	
Individual 1	32.07	50.54	29.17	35.68	21.29	17.31	9.54	14.23	
Individual 2	25.71	62.31	28.28	39.83	29.60	12.67	4.16	14.21	
Individual 3	25.48	56.21	28.20	39.85	29.92	13.87	4.28	13.75	

TABLE 11: Comparison of the dispersion of each variable obtained in those two cases $\delta = 10^\circ$ and $\delta = 20^\circ$, P wave experimental data, ($^\circ$).

	θ_1	θ_2	θ_3	θ_4	θ_5	θ_6	θ_7	θ_8	θ_9
$\Delta\theta_i$ ($\delta = 10^\circ$)	0.08	0.24	3.53	1.85	1.26	1.13	0.40	0.99	6.66
$\Delta\theta_i$ ($\delta = 20^\circ$)	1.34	11.99	9.21	3.14	8.26	11.58	1.63	0.95	11.99
	θ_{10}	θ_{11}	θ_{12}	θ_{13}	θ_{14}	θ_{15}	θ_{16}	θ_{17}	
$\Delta\theta_i$ ($\delta = 10^\circ$)	2.27	3.72	6.18	6.72	3.81	3.94	4.97	0.29	
$\Delta\theta_i$ ($\delta = 20^\circ$)	6.59	11.77	0.97	4.17	8.63	4.64	5.38	0.48	

TABLE 12: Four groups of variables in the last generation, inversion with both the P and the SV wave experimental data, ($^\circ$).

	θ_1	θ_2	θ_3	θ_4	θ_5	θ_6	θ_7	θ_8	θ_9
Individual 1	87.18	70.77	87.31	80.02	43.72	89.39	82.66	80.80	45.74
Individual 2	87.28	78.59	88.62	80.07	44.72	88.54	82.37	79.46	45.09
Individual 3	87.28	78.59	88.62	80.07	44.72	88.54	82.37	79.46	45.09
Individual 4	86.91	71.20	87.21	78.00	39.80	85.57	89.33	72.88	46.39
	θ_{10}	θ_{11}	θ_{12}	θ_{13}	θ_{14}	θ_{15}	θ_{16}	θ_{17}	
Individual 1	23.64	57.29	33.01	25.51	24.44	20.11	14.85	8.11	
Individual 2	29.26	58.70	40.98	25.06	21.80	19.27	14.85	9.26	
Individual 3	29.26	58.70	40.98	25.06	21.80	19.27	14.85	9.26	
Individual 4	28.50	58.33	41.05	28.98	25.19	18.81	14.75	8.40	

the allowed interval of each variable used in the calculation is the same as that in Table 4. After calculation, three better individuals in the last generation are presented in Table 10. The values of averaged residue sum are 8.52 mm, 9.12 mm, and 9.22 mm, respectively.

Again, the calculation result demonstrates the existence of many solutions that can solve the problem equally well. If the data in Table 9 is compared with those in Table 10, although the averaged residue sums do not change markedly, the approximate area in which each variable gathers does change noticeably. Furthermore, if the dispersion of each variable is compared between Tables 9 and 10, the result is shown in Table 11. For the case of a larger allowed interval, most of the variables have a larger dispersion also. Exception occurs again on θ_8 , θ_{12} , and θ_{13} .

The comparison of the dispersions in Tables 6 and 11 implies that good *a priori* information of the variables modeled is not only beneficial to the modeling process, but also

advantageous to the inversion calculation. When sufficient *a priori* information is gathered, it is enough to conduct an inversion algorithm within a smaller but equivalently reliable constraint space.

6.2. Inversion with Both P and SV Waves. Here in the inversion, both P and SV wave experimental data that are exhibited in Tables 7 and 8 are employed. The P wave experimental data in the table that are shaded do not take part in the calculation. The purpose is to make use of the same number of data from the P and the SV probe measurement systems. Thus, 28 pairs of experimental data are available in the inversion calculation, which produces 28 objectives.

The inversion executes 80 generations. The allowed interval of each variable is within 10° , as shown in Table 1. Similarly, variable values of four better individuals in the last generation are listed in Table 12. The averaged residue sums of the objectives are 12.92 mm, 12.96 mm, 12.96 mm,

and 13.03 mm, respectively. The reason for providing four individuals is the same as that in the inversion with P wave experimental data only.

It is observed from the averaged residue sum that no better results are achieved by including the SV wave experimental data. With running the same number of generations, the averaged residue sums are even worse than that of the inversion with only P wave data. This may be attributed to the difference between the forward simulation data and the experimental data, which is discussed at the end of Section 5. From Table 12, it is still difficult to conclude in which specific area a variable θ_i distributes. A relatively large dispersion in some variables can be noticed.

7. Concluding Remarks

An initiative to estimate the crystal orientations in an anisotropic weld is presented in this paper. It combines the power of a theoretical forward model and an inversion calculation realized by a multiobjective genetic algorithm. Experiments and inversions are performed. Simulations with synthetic data and different combination of experimental data are conducted. As a typical characteristic of a nonlinear problem, many solutions can solve the problem equally well in each simulation. Some technical points in estimating grain orientation of an anisotropic weld are discussed in the following.

- (1) The weld model: how to model a weld, which parameters should be utilized to model a weld properly, is still a problem that needs consideration. A good weld model should both fit closely to its prototype and ease later computations. The adoption of different variables in modeling a weld directly relates to the feasibility or the complexity of the whole problem.
- (2) The ray tracing algorithm: since in the inversion the simulation result is to be compared with experimental data, the quality of a ray tracing algorithm is undoubtedly an essential element that needs careful consideration. From the experience of creating a forward ray tracing model in this paper, a dynamic ray tracing [24] is recommended for future applications, especially in simulations of ultrasound propagating through an inhomogeneous, anisotropic weld.
- (3) The optimization algorithm: the multiobjective genetic algorithm used in this paper is only one practical choice. When the problem is large, its disadvantage of time-consuming execution is exposed. How to select a suitable optimization algorithm is not obvious. It needs an integrated review of the whole model, from the weld model to the forward algorithm adopted. In addition, the multiobjective genetic algorithm considers all objectives equally and makes a compromise among them. This may not be correct if some of the experimental data are less credible.

Conflict of Interests

The authors declare that there is no conflict of interests regarding the publication of this paper.

Acknowledgments

This project is partially financed by the Swedish Radiation Safety Authority (SSM) and the Swedish Qualification Center (SQC). This is gratefully acknowledged.

References

- [1] L. Wang, "Determination of the ray surface and recovery of elastic constants of anisotropic elastic media: a direct and inverse approach," *Journal of Physics: Condensed Matter*, vol. 7, no. 20, article no. 007, pp. 3863–3880, 1995.
- [2] C. Aristégui and S. Baste, "Optimal recovery of the elasticity tensor of general anisotropic materials from ultrasonic velocity data," *Journal of the Acoustical Society of America*, vol. 101, no. 2, pp. 813–833, 1997.
- [3] A. D. Degtyar and S. I. Rokhlin, "Comparison of elastic constant determination in anisotropic materials from ultrasonic group and phase velocity data," *Journal of the Acoustical Society of America*, vol. 102, no. 6, pp. 3458–3466, 1997.
- [4] J. A. Ogilvy, "Computerized ultrasonic ray tracing in austenitic steel," *NDT International*, vol. 18, no. 2, pp. 67–77, 1985.
- [5] M. Spies, "Elastic waves in homogeneous and layered transversely isotropic media: plane waves and Gaussian wave packets. A general approach," *Journal of the Acoustical Society of America*, vol. 95, no. 4, pp. 1748–1760, 1994.
- [6] K. J. Langenberg, R. Hannemann, T. Kaczorowski et al., "Application of modeling techniques for ultrasonic austenitic weld inspection," *NDT and E International*, vol. 33, no. 7, pp. 465–480, 2000.
- [7] M. Spies, "Modeling of transducer fields in inhomogeneous anisotropic materials using Gaussian beam superposition," *NDT and E International*, vol. 33, no. 3, pp. 155–162, 2000.
- [8] J. Moysan, A. Apfel, G. Corneloup, and B. Chassignole, "Modelling the grain orientation of austenitic stainless steel multipass welds to improve ultrasonic assessment of structural integrity," *International Journal of Pressure Vessels and Piping*, vol. 80, no. 2, pp. 77–85, 2003.
- [9] M. Spies, "Analytical methods for modeling of ultrasonic non-destructive testing of anisotropic media," *Ultrasonics*, vol. 42, no. 1–9, pp. 213–219, 2004.
- [10] B. Köhler, W. Müller, M. Spies et al., "Ultrasonic testing of thick walled austenitic welds: modelling and experimental verification," *AIP Conference Proceedings*, vol. 820, pp. 57–64, 2006.
- [11] K. Nakahata, S. Hirose, F. Schubert, and B. Köhler, "Image based EFIT simulation for nondestructive ultrasonic testing of austenitic steel," *Journal of Solid Mechanics and Materials Engineering*, vol. 3, no. 12, pp. 1256–1262, 2009.
- [12] B. Chassignole, R. El Guerjouma, M.-A. Ploix, and T. Fouquet, "Ultrasonic and structural characterization of anisotropic austenitic stainless steel welds: towards a higher reliability in ultrasonic non-destructive testing," *NDT & E International*, vol. 43, no. 4, pp. 273–282, 2010.
- [13] J. Zhang, A. Hunter, B. Drinkwater, and P. D. Wilcox, "Monte carlo inversion of ultrasonic array data to map anisotropic weld

- properties,” *IEEE Transactions on Ultrasonics, Ferroelectrics, and Frequency Control*, vol. 59, no. 11, pp. 2487–2497, 2012.
- [14] A. Apfel, J. Moysan, G. Corneloup, T. Fouquet, and B. Chassignole, “Coupling an ultrasonic propagation code with a model of the heterogeneity of multipass welds to simulate ultrasonic testing,” *Ultrasonics*, vol. 43, no. 6, pp. 447–456, 2005.
- [15] C. Gueudre, L. le Marrec, J. Moysan, and B. Chassignole, “Direct model optimisation for data inversion. Application to ultrasonic characterisation of heterogeneous welds,” *NDT and E International*, vol. 42, no. 1, pp. 47–55, 2009.
- [16] Q. Liu and H. Wirdelius, “A 2D model of ultrasonic wave propagation in an anisotropic weld,” *NDT and E International*, vol. 40, no. 3, pp. 229–238, 2007.
- [17] H. Wirdelius, G. Persson, K. Hamberg, and K. Högberg, “ULIAS4-experimental validation of a software that models ultrasonic wave propagation through an anisotropic weld,” SKI Report 2008:05, 2008.
- [18] B. A. Auld, “General electromechanical reciprocity relations applied to the calculation of elastic wave scattering coefficients,” *Wave Motion*, vol. 1, no. 1, pp. 3–10, 1979.
- [19] J. A. Ogilvy, “A model for elastic wave propagation in anisotropic media with applications to ultrasonic inspection through austenitic steel,” *British Journal of Non-Destructive Testing*, vol. 27, no. 1, pp. 13–21, 1985.
- [20] S. R. Kolkoori, M.-U. Rahaman, P. K. Chinta, M. Kreutzbruck, and J. Prager, “Quantitative evaluation of ultrasonic sound fields in anisotropic austenitic welds using 2D ray tracing model,” in *Proceedings of the 38th Annual Review of Progress in Quantitative Nondestructive Evaluation (QNDE '11)*, pp. 1227–1234, July 2012.
- [21] Q. Liu, *Optimal estimation of crystal orientations in a stratified structure using ultrasonic techniques [Ph.D. thesis]*, Chalmers University of Technology, 2007.
- [22] K. Deb, *Multi-Objective Optimization Using Evolutionary Algorithms*, Wiley, Chichester, UK, 2001.
- [23] K. Deb, A. Pratap, S. Agarwal, and T. Meyarivan, “A fast and elitist multiobjective genetic algorithm: NSGA-II,” *IEEE Transactions on Evolutionary Computation*, vol. 6, no. 2, pp. 182–197, 2002.
- [24] Červený V., *Seismic Ray Theory*, Cambridge University Press, Cambridge, UK, 2001.



Hindawi

Submit your manuscripts at
<http://www.hindawi.com>

